Compatibility Assessment of Multistatic/Polarimetric Clutter Data with the SIRP Model

Aubry, Augusto; Carotenuto, Vincenzo; De Maio, Antonio; Fioranelli, Francesco

DOI
10.1109/TAES.2022.3184916

Publication date
2023

Document Version
Final published version

Published in
IEEE Transactions on Aerospace and Electronic Systems

Citation (APA)
Aubry, A., Carotenuto, V., De Maio, A., & Fioranelli, F. (2023). Compatibility Assessment of Multistatic/Polarimetric Clutter Data with the SIRP Model. *IEEE Transactions on Aerospace and Electronic Systems*, *59*(1), 359-374. https://doi.org/10.1109/TAES.2022.3184916

Compatibility Assessment of Multistatic/Polarimetric Clutter Data With the SIRP Model

AUGUSTO AUBRY, Senior Member, IEEE
VINCENZO CAROTENUTO, Senior Member, IEEE
ANTONIO DE MAIO, Fellow, IEEE
University of Naples Federico II, Naples, Italy

FRANCESCO FIORANELLI, Senior Member, IEEE
Delft University of Technology, Delft, The Netherlands

This article deals with the statistical inference of simultaneously recorded co- and cross-polarized bistatic coherent sea-clutter returns at *S*-band. This study is conducted employing appropriate statistical learning tools, involving the complex envelope of data, to assess the compliance of the available measurements with the spherically invariant random process (SIRP) representation, as well as to analyze possible texture correlations among the diverse polarimetric channels. Moreover, the spatial heterogeneity of the sea-clutter data is studied. The results highlight that the SIRP model is a good candidate for the representation of bistatic coherent clutter and usually the coherence time of the SIRP texture at the bistatic nodes is longer than that in the monostatic sensing. Notably, at bistatic angles in order of 60°, the quadrature components of the cross-polarized bistatic measurements substantially exhibit a Gaussian behavior. These achievements further shed light on the bistatic sea-clutter diversity from the geometric and polarimetric point of view.

Manuscript received 10 November 2021; revised 21 March 2022 and 6 June 2022; accepted 11 June 2022. Date of publication 21 June 2022; date of current version 10 February 2023.

DOI. No. 10.1109/TAES.2022.3184916

Refereeing of this contribution was handled by L. Rosenberg.

The work of Augusto Aubry and Antonio De Maio was supported by the research project SCN_00393 "S4E - Sistemi di sicurezza e protezione per l'Ambiente Mare." The work of Vincenzo Carotenuto was supported by the research program PON R&I AIM1878982-1.

Authors' addresses: Augusto Aubry, Vincenzo Carotenuto, and Antonio De Maio are with the University of Naples Federico II, 80138 Naples, Italy, E-mail: (augusto.aubry@unina.it; vincenzo.carotenuto@unina.it; ademaio@unina.it); Francesco Fioranelli is with the Department of Microelectronics, Delft University of Technology, 2628RG Delft, The Netherlands, E-mail: (f.fioranelli@tudelft.nl). *(Corresponding author: Vincenzo Carotenuto.)*

I. INTRODUCTION

Many adaptive radar signal processing schemes (especially those focused on detection) require a preliminary statistical inference on the environment surrounding the radar. Deviations between the design and the actual clutter statistical properties may cause considerable performance degradation of the algorithm. This is particularly true for maritime applications involving high-range-resolution systems and/or operation at low grazing angles where, due to the impulsive behavior of the sea-clutter, the Gaussian model is not usually appropriate for the statistical characterization of the clutter returns.

During the past decades, the problem of identifying suitable statistical models for sea-clutter has attracted the interest of many scientists. In this respect, based on experimental evidence on measurements collected by radar systems operating in a monostatic configuration, a widely recognized statistical framework to describe sea-clutter relies on the use of compound Gaussian (CG) distributions [1]–[16]. This is tantamount to representing the clutter backscattering as the product of two statistically independent stochastic processes commonly referred to as texture and speckle. The speckle models the underlying background (scatterers over a large area, i.e., the Bragg scattering) and the texture characterizes the modulation of that background due to long-period waves. Furthermore, if the texture stochastic process can be approximated as a random variable over an appropriate time interval (referred to as the coherence time), then the CG model boils down to a spherically invariant random process (SIRP) [3], namely a zero-mean Gaussian process with a stochastic variance. Although the physical processes behind sea-clutter are very complex (including specular reflections, shadowing, multipath, and sea spray), the SIRP model has been widely used for sea-clutter statistical characterization, especially for monostatic radar. This is due to the fact that it allows analytic tractability, which is very useful both for the design of radar detectors as well as for their performance analysis. Moreover, it includes the Gaussian clutter model (obtained forcing a deterministic texture) as a special case. Of course, as all the analytic models, it presents some limitations. Among them a SIRP is not ergodic, usually assumes a wide-sense stationary speckle component (with resulting issues in modeling time-varying spectra), and does not (in general) account for the joint presence of clutter and thermal noise.

For radars operating in multistatic/polarimetric configuration, sea-clutter statistical characterization in terms of a SIRP is not fully explored, especially with reference to higher order statistics. Indeed, the so called clutter diversity [17], [18], namely the variation of the sea-clutter features with respect to the acquisition geometry, sea state, antenna polarization used at transmit/receive side (just to mention a few), makes the study more difficult and challenging [18], [19]. In this respect, an important instrument to foster a better understanding of the bistatic sea-clutter diversity

as well as to characterize the differences between monostatic and bistatic clutter echoes is represented by the netted radar (NetRAD) system [20]. The most relevant datasets collected using NetRAD refer to measurement campaigns conducted in October 5, 10, and 21, 2010 and in June 7 and 9, 2011. Exploiting these acquisitions, relevant bistatic sea-clutter characteristics, such as radar cross section, amplitude statistics, Doppler spectra, and data correlation properties have been assessed in the open literature [20]–[35]. In the following, some key achievements from these studies are summarized.

In [29], using the data from 5 and 10 October, the authors observed that, for most of the analyzed measurements, the model providing the best fit with the clutter amplitude is the KA distribution with model parameters depending upon the sea-clutter spikiness. Moreover, the monostatic clutter appeared more spiky than the bistatic counterpart especially for the horizontal polarized configuration and values of the bistatic angle close to 90°. In [30], using the measurements from 10 and 21 October, a statistical analysis of clutter amplitude and sea spikes show that spikiness is stronger for small bistatic angles, and that bistatic clutter returns are in general less spiky than the monostatic counterpart for horizontal polarization. In [31], resorting to data collected in October 2010 and modeling the clutter amplitude statistics according to a K-distribution, the authors observed that the shape parameter of the Gamma texture for the horizontal co-polarized bistatic data monotonically increases with the bistatic angle. On the contrary, for the vertical co-polarized situation the value of the shape parameter increase from bistatic angles 60° to 90° and then reduce from 90° to 120°. Moreover, they highlighted that also the Doppler features of the bistatic returns change with polarization and acquisition geometry. In [32], the authors described a measurement campaign conducted in June 9, 2011 where, differently from the datasets acquired in 2010, two bistatic sensors were employed to simultaneously collect both co- and cross-polarized sea-clutter returns. In addition, they conducted a statistical characterization of the measurements observing that the cross-polarized bistatic data tend to be less spiky than the co-polarized monostatic and bistatic data.

To the best of the authors' knowledge, with the exception of [32], the statistical analyses conducted using NetRAD measurements have been mainly performed by only considering one active and one passive node, namely without investigating the behavior of simultaneously collected co- and cross-polarized bistatic data. Moreover, the statistical studies from the open literature largely focus on first-order statistics (clutter amplitude) and/or Doppler spectrum inferences. As such a higher order statistical analysis of multistatic/polarimetric sea-clutter returns using the complex envelope of the available data is not yet present. This is undoubtedly of primary concern for the development of multivariate data models necessary for the radar detector design process. Moreover, it may corroborate the already experimentally observed clutter diversity features.

Within this frame of reference, the goal of this article is to fill the mentioned gap and to assess the compatibility of simultaneously collected co- and cross-polarized multistatic sea-clutter returns with the SIRP model using the complex envelope of the available data.[1] More in detail, necessary conditions for the data to comply with the SIRP representation are tested via the Kolmogorov–Smirnov (KS) test [37], which allows the assessment of the goodness-of-fit between an empirical and a theoretical distribution. Both first- and higher order statistics (i.e., multivariate probability density function of clutter samples) are considered involving also the representation of an L-dimensional data vector in terms of generalized spherical coordinates. Moreover, a Cramer–Von Mises (CV) test [37] is exploited to study the local Gaussian behavior of the sea clutter and to get estimates of the coherence time. Last but not least a study on the spatial heterogeneity of the sea-clutter as well as on the texture correlation among cross-channels is conducted.

The main achievements obtained from the statistical analysis conducted on the considered NetRAD data can be summarized as follows:

1) Both the monostatic and the bistatic sea-clutter data adhere well with the SIRP representation.
2) The coherence time for the monostatic measurements is, in general, smaller than the bistatic counterparts regardless of the polarization configuration.
3) For both the horizontal and vertical co-polarized scenarios, at the passive side the estimated coherence time is smaller than the cross-polarized counterparts.
4) Regardless of the acquisition geometry (i.e., bistatic angle) and the polarization at the active and passive sensors, the coherence time estimated using bistatic measurements decreases as the bistatic angle increases from 90° to 105°.
5) Regardless of the bistatic angle and the transmit polarization, the bistatic sea-clutter returns collected using the horizontal-polarized node exhibit lower power levels than the vertical polarized acquisitions.
6) Using horizontal transmit polarizion, for values of bistatic angle smaller than or equal to 90° the standardized textures over the cross-polarized bistatic channels can be deemed almost the same. Conversely, for the vertical-polarized transmit mode the opposite trend is observed, i.e., the standardized textures are quite diverse.
7) Regardless of the transmit polarization, the similarity of the standardized textures over the cross-polarized bistatic channels increases as the bistatic angle increases from 95° to 105°.

The rest of this article is organized as follows. Section II is devoted to a short description of the radar system and the geometry used to collect the data. In Section III, the signal processing tools adopted to learn bistatic sea-clutter returns statistical properties are introduced. In Section IV,

[1]Preliminary results on this study are shown in [36].

range and polarimetric heterogeneity are analyzed. In Section V, the aggregate results of the conducted analysis are discussed. Finally, Section VI concludes this article.

Notation: In the rest of this article, vectors and matrices are denoted by boldface lower case letters ($\boldsymbol{a}$) and upper case letters ($\boldsymbol{A}$), respectively. The nth element of $\boldsymbol{a}$ is denoted by $a(n)$. The transpose operator is denoted by the symbol $(\cdot)^T$. The letter j represents the imaginary unit (i.e., $j = \sqrt{-1}$). The real part, the imaginary part, and the modulus of the complex number x are denoted by $\Re\{x\}$, $\Im\{x\}$, and $|x|$, respectively. $\mathcal{P}(\cdot)$ denotes either the real or the imaginary part of the argument. The acronym iid stands for independent and identically distributed. If x is a real-valued random variable, $x \sim \mathcal{U}(a, b)$ means that x is uniformly distributed in the interval (a, b), $x \sim \mathcal{C}(0, 1)$ indicates that x is distributed according to a standard Cauchy, whereas $x \sim \mathcal{N}(0, \sigma^2)$ denotes that x is Gaussian-distributed with zero-mean and variance σ^2. If x is a complex-valued random variable, $x \sim \mathcal{CN}(0, \sigma^2)$ means that x is zero-mean circularly-symmetric complex Gaussian with variance σ^2. Finally, the symbol $\wedge$ represents the logical AND operation.

II. NETRAD SYSTEM AND DATASET DESCRIPTION

In this section, a brief overview of the radar system used to collect data along with a description of the considered datasets are provided. Measurements were gathered using the NetRAD system, which is an S-band ground-based multistatic polarimetric sensing system allowing the simultaneous collection of both monostatic and bistatic radar returns.[2] It was initially developed by the University College London (UCL) and successively modified via a joint collaboration between UCL and the University of Cape Town (UCT), obtaining separate active and passive nodes with baselines in the order of kilometer. This was achieved synchronizing the entire system using GPS disciplined oscillators (GPSDOs) at each node, thus avoiding cabled connections (as in the original version of the NetRAD) and granting more degrees of freedom in terms of baselines among nodes.

During the last years, the NetRAD was used to conduct several measurement campaigns involving different system setups, in terms of number of nodes, transmit power, acquisition geometry, and features of the probing signal, just to list a few [20]–[35], [39]. Moreover, data were also acquired under different environmental conditions, i.e., sea state, wind speed, wind direction, and so on. As a follow on to the NetRAD, the UCT and UCL recently developed the NeXtRAD, which is still a multistatic/polarimetric system but operates over the L- and X-bands [40].

Data exploited in this article were collected using NetRAD on June 9, 2011 in South Africa at Misty Cliffs using the following three nodes: one active (with transmit and receive capabilities) and two passive [32]. The passive nodes were co-located and used to measure the bistatic sea-clutter returns from both the horizontal and the vertical polarization. Additionally, they were separated from the active sensor via a baseline of 1830 m. As to the active node, it was a pulsed radar operating over a carrier frequency of 2.4 GHz, transmitting linear up-chirp waveforms with a swept bandwidth of 45 MHz (i.e., a range resolution of 3.3 m), and a pulse repetition frequency (PRF) equal to 1 kHz. For each experiment, the pulse duration was changed from 1.8 to 3 μs depending on the acquisition geometry (bistatic angle, β). Finally, the antennas used for both the active and passive nodes had approximately 24 dBi gain and 10° beamwidth both in azimuth and elevation. Table I summarizes the main parameters involved into the considered measurement campaign.

TABLE I
Radar Parameters

Parameter	Value
Carrier frequency	2.4 GHz
Peak power	450 W
Modulation	Linear up-chirp
Pulse bandwidth	45 MHz
Pulse duration	1.8–3 μs
PRF	1 kHz
Antenna gain	24 dBi
Antenna beamwidth	10° (azimuth/elevation)
Baseline	1830 m

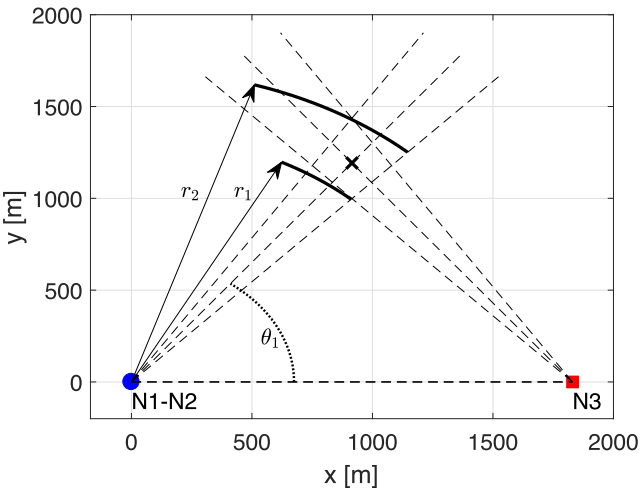

Fig. 1. System geometry for $\beta = 75°$. N3 represents the monostatic node, N1–N2 are the two co-located bistatic sensors.

As to the acquisition geometry, the experiment was conducted on the west side of the Cape Peninsula with the sensors facing the Atlantic Ocean. As shown in Fig. 1, the antennas were steered so that the intersection point between the boresight of the transmitting/receiving antennas ($\times$-marked point) and the position of the nodes ($\circ$- and $\square$-marked points) occupy the vertices of an isosceles triangle with axis of symmetry perpendicular to the baseline between the two co-located passive nodes (N1–N2) and the monostatic sensor (N3). The passive nodes N1 and N2 collected data from the H and V polarization, respectively. At N3, the transmit and receive polarizations were changed during the measurement campaign.

Different bistatic angles equal to 60°, 75°, 90°, 95°, 105°, and 120°, were considered by pointing the antennas at the transmit and the receive sides to a common clutter

[2]According to [38], the NetRAD system can be also referred to as a hybrid radar equipped with polarimetric diversity capabilities.

TABLE II
Polarization Configurations for the Available Measurements

Dataset number	Pol. N3 (Tx–Rx)	Pol. N1 (Rx)	Pol. N2 (Rx)	β [deg]	τ [μs]	δr [m]
1	HH	H	V	60	3	568
2	HH	H	V	75	3	347
4	HH	H	V	90	2.2	228
5	HH	H	V	95	2.2	200
6	HH	H	V	105	1.8	155
7	HH	H	V	120	1.8	107
8	VH	H	V	60	3	568
9	VH	H	V	75	3	347
11	VH	H	V	90	2.2	228
12	VH	H	V	95	2.2	200
13	VH	H	V	105	1.8	155
14	VH	H	V	120	1.8	107

patch exploiting optical telescopic sights and turntables. The common clutter patch corresponds to the area where transmitter and receiver antenna patterns intersect. In particular, owing to the acquisition setup symmetries (both in terms of geometry and Tx–Rx radiation patterns), the minimum and maximum distance r_1 and r_2 of the clutter patch from N1 and N2 can be computed as [26], [34]

$$r_1 = (\delta_B/2)\cos(\theta_{3\,\mathrm{dB}}/2)/\cos(\theta_1 - \theta_{3\,\mathrm{dB}}/2)$$
$$r_2 = (\delta_B/2)\cos(\theta_{3\,\mathrm{dB}}/2)/\cos(\theta_1 + \theta_{3\,\mathrm{dB}}/2) \quad (1)$$

where δ_B denotes the baseline, $\theta_{3\,\mathrm{dB}}$ is the angular width of the antenna's main lobe (in azimuth), and θ_1 is the pointing angle in the azimuth direction. Notably, $[r_1, r_2]$ also identifies the monostatic, i.e., with respect to N3, range swath of the clutter patch of interest.

Table II summarizes the polarization configurations associated with each dataset along with the corresponding pulse duration (τ) of the waveform transmitted by N3 and the range swath of the clutter patch evaluated as $\delta r = r_2 - r_1$. The reported values highlight that δr decreases as β increases. This is due to the specific acquisition geometry employed for the NetRAD to collect the data.

For all the mentioned acquisition scenarios, measurements refer to a time span of 130 s which, with a PRF of 1 kHz, corresponds to $N_s = 130\,000$ slow-time samples for each range cell. Thus, for a specific range bin, the baseband complex envelope of the bistatic sea-clutter returns for the dth dataset, $d \in D = \{1, 2, 4, 5, 6, 7, 8, 9, 11, 12, 13, 14\}$, at the sensor i, $i = 1, 2, 3$, can be expressed as[3]

$$\tilde{z}_{d,i}(n) = \tilde{z}^I_{d,i}(n) + j\tilde{z}^Q_{d,i}(n), \quad n = 1, \ldots, N_s \quad (2)$$

where $\tilde{z}^I_{d,i}(n)$ and $\tilde{z}^Q_{d,i}(n)$ denote the in-phase (I) and quadrature (Q) components, respectively. For the available measurements, the clutter-to-noise ratio (CNR) depends on the range cell position within the clutter patch, as well as on the polarization pair and the bistatic angle. In particular, the average CNR (computed on the clutter bandwidth) over the ranges of interest is between 8 and 30 dB.

Finally, as to the environmental conditions, the wind speed/direction and wave height/direction remained almost constant during the experiments. Specifically, the wind speed was about 8–9 m/s blowing from the south–south–east direction, whereas the wave height and direction were ≈ 2 m (sea state 4) and $\approx 225^\circ$ with respect to the true north, respectively.

Before proceeding with data analysis, in the following section some preprocessing operations performed on the available sea-clutter returns are described.

A. Signal Conditioning

As discussed in the previous section, the synchronization of the sensors in the NetRAD system is realized using three GPSDOs. Since these oscillators are independent, there could be differences both in terms of start triggers and oscillation frequencies. Such undesired effects lead to range misalignments and deviations of the relative phase between the signals collected at the different nodes. Both issues are accounted for by exploiting the sidelobe-to-sidelobe direct signal, i.e., the signal in line-of-sight transmitted through the sidelobes of the transmit antenna and received through the sidelobes of the antenna at the bistatic sensors[4] [20]. In a nutshell, the sidelobe-to-sidelobe signal can be regarded at the bistatic nodes as the echo associated with a stationary target located at a bistatic range equal to the baseline. Thus, any variation in the phase of this signal can be ascribed to the receive oscillator instability.

Precisely, since the active node is located at a known distance with respect to the passive sensors:

1) range offset, due to the GPSDOs imperfections (as well as other electronic components), is determined by subtracting the range delay resulting from the measurements of the sidelobe-to-sidelobe signal to the nominal value. This quantity is subsequently used to align the measurements in the time-domain with respect to the same reference signal [20];
2) phase correction, due to oscillators instabilities, is performed exploiting the sidelobe-to-sidelobe signal for calibration purposes. Specifically, at each PRI, the phase of the I/Q samples of any range bin is compensated for that measured on the sidelobe-to-sidelobe signal [20], whose range bin is easily established as that where the maximum signal strength (after pulse compression) is present.

After applying the mentioned corrections, unless otherwise stated, for each node and range cell belonging to the clutter patch, a standardization procedure is applied to the slow-time measurements so as to remove dc offset and normalize to the data standard deviation (for both I and Q component). Precisely, for each range bin the following data vector is considered

$$z_{d,i}(n) = z^I_{d,i}(n) + jz^Q_{d,i}(n)$$

[3]In the following, for notation simplicity for a given dataset the index corresponding to different range bins is omitted.

[4]This signal is also referred to as sidelobe or direct breakthrought.

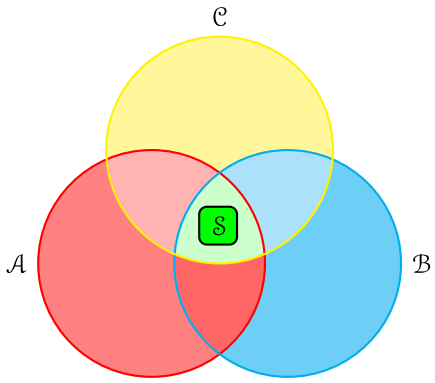

Fig. 2. Notional illustration of the rationale behind the proposed statistical analysis: $\mathcal{A}$ encompasses the quadrature components ratio samples with a Cauchy distribution, $\mathcal{B}$ corresponds to complex samples with a Uniform phase distribution, and $\mathcal{C}$ includes the generalized spherical components with a specific multivariate distribution.

$n = 1, \ldots, N_s$, $i = 1, 2, 3$, $d \in D$, with

$$z^I_{d,i} = \frac{\tilde{z}^I_{d,i} - \hat{\mu}^I_{d,i}}{\hat{\sigma}^I_{d,i}}, \quad z^Q_{d,i} = \frac{\tilde{z}^Q_{d,i} - \hat{\mu}^Q_{d,i}}{\hat{\sigma}^Q_{d,i}}$$

where $\hat{\mu}^P_{d,i}$ and $\hat{\sigma}^P_{d,i}$, $P \in \{I, Q\}$, denote the sample mean and standard deviation of $\tilde{z}^P_{d,i}$, respectively. Moreover, a possible imbalance between the quadrature channels is removed according to the procedure specified in [41].

III. COMPATIBILITY WITH THE SIRP MODEL

Let us denote by $z_{d,i}(t)$, $d \in D$, $i = 1, 2, 3$, the continuous-time version of (2). If this signal complies with the CG model, then it can be represented as the product of two statistically independent stochastic processes, namely as [3], [42], [43]

$$z_{d,i}(t) = s_{d,i}(t) g_{d,i}(t), \quad d \in D, \ i = 1, 2, 3 \tag{3}$$

where $s_{d,i}(t)$ is a slowly varying nonnegative component and $g_{d,i}(t)$ is a zero-mean complex circular Gaussian process. They are commonly referred to, in the open literature, as texture and speckle, respectively. Interestingly, if the texture stochastic process can be approximated as a random variable over an appropriate time interval T_c, referred to as the coherence time, the CG model in (3) becomes

$$z_{d,i}(t) = s_{d,i} g_{d,i}(t), \quad d \in D, \ i = 1, 3, \ t \in T_c \tag{4}$$

which is a SIRP [3]. Let us observe that any finite set of an arbitrary number of temporal samples from (4) is a spherically invariant random vector (SIRV). Hence, the compatibility of the sea-clutter from a given range cell with the SIRP model can be assessed by studying the adherence of the aforementioned random vectors with the SIRV model.

Following the methodology proposed in [12], this task is accomplished using the complex envelope of the available sea-clutter data. A notional illustration of the rationale behind the proposed statistical analysis is sketched in Fig. 2. Therein, the green box $\mathcal{S}$ is representative of the SIRV distributions family,[5] whereas the circles refer to families of multivariate probability distributions complying with specific statistical properties. More in detail, the red and the blue circles ($\mathcal{A}$ and $\mathcal{B}$, respectively) refer to a first-order statistical characterization:

1) $\mathcal{A}$ encompasses complex random vectors where the ratio between the quadrature components of each sample is modeled as a Cauchy random variable.
2) $\mathcal{B}$ corresponds to random vectors whose complex samples exhibit phases with a uniform distribution over the interval $(0, 2\pi)$.

Besides, the yellow circle $\mathcal{C}$ includes the family of distributions presenting a specific characterization of the generalized spherical coordinates associated with the random vector elements. Now, since SIRVs simultaneously belong to all the aforementioned classes of distributions, they lay in the intersection of the three clusters. As a consequence, data compliance with the SIRV model demands as a necessary condition that specific statistics extracted from the random vector satisfy some structural properties characterizing the red, blue, and yellow classes. Hence, the aim of the following sections is to conceive statistical tools capable of establishing the compatibility of the data with all the classes with theoretical guarantees on the reliability of the test.

In this respect, for a given range bin, both first-order and higher order statistical tests have been implemented as explained in the following sections along with some illustrative examples related to the measurements from set 1. In all the developed analyses, let us observe that the decision thresholds involved in both KS and CV test (to establish whether the null hypothesis can be retained or rejected) do not depend on the tested distribution. Such values are available in table formats for different significance levels [12], [37].

A. First-Order Statistics

Let us observe that if the available data fits the SIRV model, the ratio between the quadrature components has to follow a standard Cauchy distribution [12]. Hence, a necessary requirement for the complex envelope to comply with the SIRP model is provided by the following hypotheses:

$$\begin{aligned} H_0 : \ R_{d,i}(n) &= \frac{z^I_{d,i}(n)}{z^Q_{d,i}(n)} \sim \mathcal{C}(0, 1) \\ H_0 : \ \bar{R}_{d,i}(n) &= \frac{z^Q_{d,i}(n)}{z^I_{d,i}(n)} \sim \mathcal{C}(0, 1) \end{aligned} \tag{5}$$

$d \in D$, $i = 1, 2, 3$, and $n = 1, \ldots, N_s$. Besides, if the complex envelope is a SIRP, then it must comply with the circular symmetry property, i.e., the amplitude and the phase of the collected signal samples must be statistically independent, with the phase following a uniform distribution

[5] A specific instance of the SIRV model requires setting out the statistical distribution of the texture component and the speckle covariance matrix.

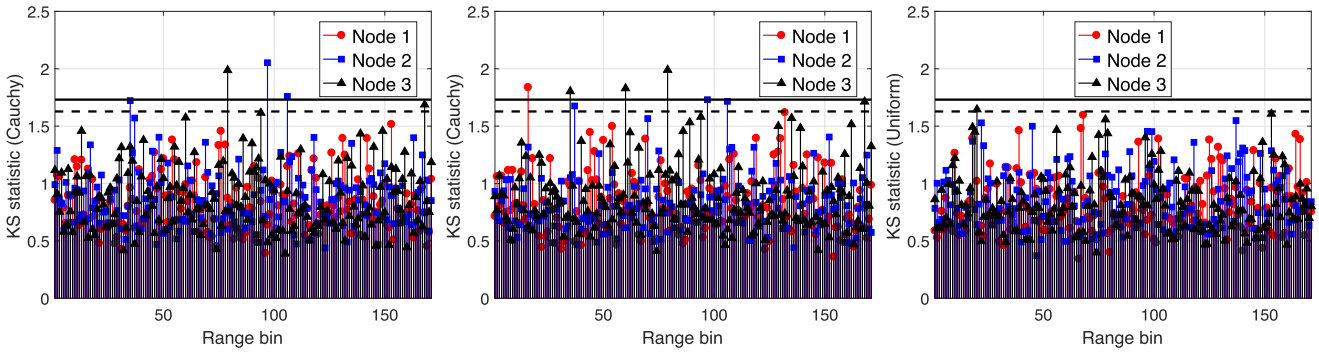

Fig. 3. KS statistics associated with $R_{1,i}$ (a), $\bar{R}_{1,i}$ (b), and $\phi_{1,i}$ (c), $i = 1, 2, 3$.

over the interval $(0, 2\pi)$. Hence, a further evidence on the compatibility of sea-clutter returns with the SIRP model can be obtained by testing the following simple hypothesis:

$$H_0 : \ \phi_{d,i}(n) = \text{atan}_{IV}\left[\frac{z^Q_{d,i}(n)}{z^I_{d,i}(n)}\right] \sim \mathcal{U}(0, 2\pi) \qquad (6)$$

$d \in D, i = 1, 2, 3$, and $n = 1, \ldots, N_s$, where $\text{atan}_{IV}(\cdot)$ is the four-quadrant inverse tangent function [12]. Moreover, let us observe that if $\phi_{d,i} \sim \mathcal{U}(0, 2\pi)$, $d \in D$, $i = 1, 2, 3$, then the corresponding kurtosis and skewness are -1.2 and 0, respectively. As a consequence, to further corroborate the adherence of the signal phase with the uniform distribution, it is also possible to verify that the corresponding kurtosis and skewness agree with the expected theoretical values.

Requirements in (5) and (6) can be studied resorting to the Kolmogorov–Smirnov (KS) test [37] that allows the assessment of the goodness-of-fit between the empirical distribution with the corresponding theoretical counterparts. However, the KS test requires independent observations. Thus, before evaluating the KS statistics the available sea-clutter returns have been decimated in the slow-time domain to ensure almost uncorrelated, and hopefully independent, speckles for both the I and Q components. The decimation factor has been set according to the estimated decorrelation time of 0.05 s (i.e., 50 samples at PRF of 1 kHz). Thus, for each range bin belonging to the clutter patch, 2600 samples have been used to evaluate the KS statistics. For all the considered datasets, the decimation process ensures an average one-lag correlation coefficient of the analyzed data smaller than 0.2.

Fig. 3 illustrates the KS statistics associated with $R_{1,i}$, $\bar{R}_{1,i}$, and $\phi_{1,i}$, $i = 1, 2, 3$, compared with the testing threshold 1.628 (dashed line) and 1.731 (solid line) corresponding to 0.01 and 0.005 significance levels, respectively. Inspection of the subplots pinpoints that for both the monostatic and bistatic measurements, most of the range bins agrees with the null hypotheses in (5) and (6). In particular, Table III reports the range bins corresponding to the KS statistics that exceed the decision threshold at 0.01 significance level. Interestingly, the tests on R and $\bar{R}$ indicate almost the same range bins where the hypothesis of a standard Cauchy distribution can be rejected. As to the phase sequences, instead, the analysis suggests that the hypothesis of uniform phase cannot be rejected for all the available bistatic measurements whereas for the monostatic returns only one range bin exceeds the threshold.

TABLE III
Range Bins for Dataset 1 Where the First-Order KS Statistics Exceed the Threshold, for a 0.01 Significance Level

Node	R	$\bar{R}$	ϕ
1	-	16	-
2	35, 97, 106	37, 97, 106	-
3	79, 168	35 60, 79, 168	20

As a further confirmation of the previous results, Fig. 4 shows the ECDF of the sequence warped according to the underlying distribution. By doing so, if the test statistics $R_{1,i}$ and $\bar{R}_{1,i}$, $i = 1, 2, 3$, agree with the respective null hypothesis, the resulting curve has to resemble a straight line over [0,1]. In particular, for each node and for each test statistic, this analysis is conducted considering two range bins, one exceeding the testing threshold and another one where the null hypothesis cannot be rejected (range bin 85, namely the center of the clutter patch). The figures show that for the range bins fulfilling the null hypothesis the ECDFs follow the expected trend. Conversely, when the threshold is exceeded some deviations from the theoretical behavior are experienced.

Before concluding this section, let us observe that to make inference on the compliance of the sea-clutter returns associated to a specific range bin with the SIRP model, both the null hypotheses in (5) and (6) have to be fulfilled (they are all necessary conditions for the SIRP assumption). In this respect, Table IV reports the percentage of range bins for which, at a 0.01 significance level, the considered null hypotheses cannot be rejected. Precisely, the first three rows refer to $R_{1,i}$, $\bar{R}_{1,i}$, and $\phi_{1,i}$, $i = 1, 2, 3$, whereas the last one reports the percentage of range bins where the first-order compatibility hypothesis cannot be rejected for any of the three aforementioned tests.

Summarizing, with reference to the dataset 1 and according to the considered first-order statistics, most of the

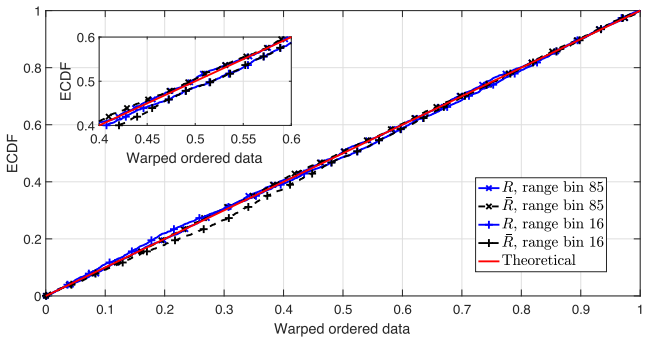

(a)

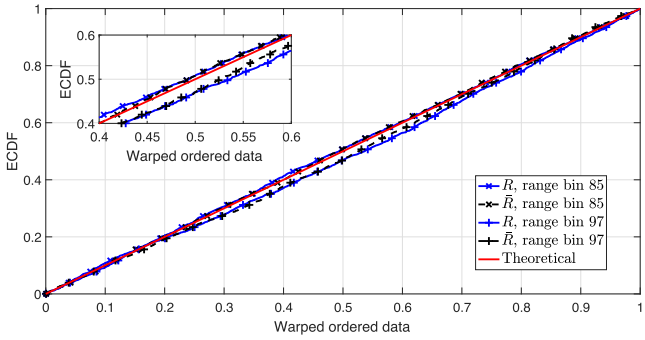

(b)

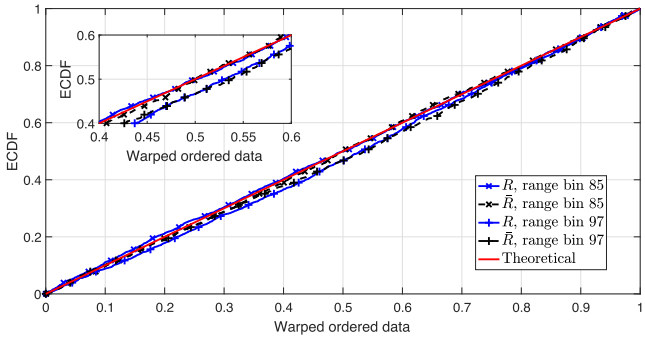

(c)

Fig. 4. ECDF of the data warped according to the underlying distribution for N1 (a), N2 (b), and N3 (c), for dataset 1.

TABLE IV
Percentage of Range Bins for Dataset 1 Where Using First-Order Statistics the SIRP Assumption Cannot Be Rejected for a 0.01 Significance Level

Test	N1	N2	N3
R	100	98	99
$\bar{R}$	99	98	98
ϕ	100	100	99
$R \wedge \bar{R} \wedge \phi$	99	98	97

sea-clutter returns for both monostatic and bistatic acquisitions exhibit a good first-order agreement with the SIRP model. A similar conclusion is drawn in Section V for the other datasets.

B. Higher Order Statistics

To formulate higher order necessary conditions about the compliance of the available data with the SIRP model it is possible to exploit the representation of a real-valued SIRV in terms of generalized spherical coordinates. Moreover, it is also of primary concern to estimate the time scale where the texture can be approximated as a random constant (i.e., the coherence time) corresponding to a local Gaussian model for the sea-clutter returns.

1) *Generalized Spherical Coordinates:* Let us preliminary observe that if $\boldsymbol{x} = [x_1, \ldots, x_L]^T$ is an L-dimensional real-valued zero-mean SIRV with identity covariance matrix, assuming $L = 5$ (this is not a limitation but coincides with the value assumed for the subsequent analysis) its generalized spherical coordinates $(R, \varphi_1, \varphi_2, \ldots, \varphi_4)$ are related to the rectangular ones through the equations

$$\begin{aligned} R &= \|\boldsymbol{x}\| \\ \varphi_1 &= \cos^{-1}\left(\frac{x_5}{R}\right) \\ \varphi_2 &= \cos^{-1}\left(\frac{x_4}{\sqrt{R^2 - x_5^2}}\right) \\ \varphi_3 &= \cos^{-1}\left(\frac{x_3}{\sqrt{R^2 - x_5^2 - x_4^2}}\right) \\ \varphi_4 &= \operatorname{sign}(x_1)\cos^{-1}\left(\frac{x_2}{\sqrt{R^2 - x_5^2 - x_4^2 - x_3^2}}\right) \\ &\quad - \pi\left(\operatorname{sign}(x_1) - 1\right). \end{aligned} \tag{7}$$

Besides, the angular coordinates $\varphi_k, k = 1, \ldots, 4$, are independent of each other as well as of the radius R, and their CDFs are given by

$$\begin{aligned} F_{\varphi_1}(\eta) &= \frac{3}{4}\left(\frac{1}{3}\cos^3\eta - \cos\eta + \frac{2}{3}\right), \quad 0 \le \eta \le \pi \\ F_{\varphi_2}(\eta) &= \frac{1}{\pi}\left(\eta - \sin\eta\cos\eta\right), \quad 0 \le \eta \le \pi \\ F_{\varphi_3}(\eta) &= \frac{1}{2}\left(1 - \cos\eta\right), \quad 0 \le \eta \le \pi \\ F_{\varphi_4}(\eta) &= \frac{1}{2\pi}\eta, \quad 0 \le \eta \le 2\pi. \end{aligned} \tag{8}$$

In other words, the joint distribution of the phases is functionally independent on the texture parameters. This permits to formulate necessary conditions for the compliance with the SIRV model without the need of doing any inference on the texture distribution.

Accordingly, for a given dataset and node, using the I or Q data after the decimation procedure discussed in Section III-A, segmenting them in subvectors of length 5, and evaluating $\varphi_1, \ldots, \varphi_4$, via (7), the compatibility with the SIRV model can be analyzed. Specifically, multiple KS tests can be performed to assess the goodness-of-fit between the empirical distributions of the phases associated with the generalized spherical representation and their theoretical counterparts in (8). This is tantamount to jointly testing the simple hypotheses

$$H_{0,k} : \varphi_{d,k,i} \text{ has the CDF } F_{\varphi_{k,d,i}}, \quad k = 1, \ldots, 4 \tag{9}$$

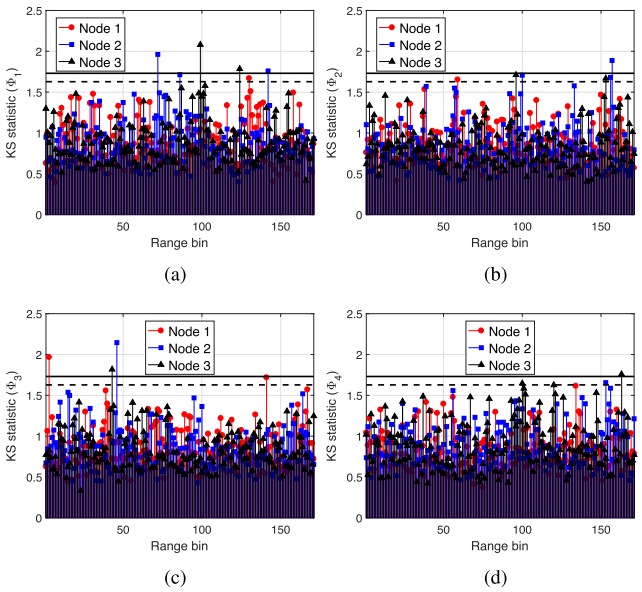

Fig. 5. KS statistics associated with $\varphi_{1,1,i}$ (a), $\varphi_{1,2,i}$ (b), $\varphi_{1,3,i}$ (c), and $\varphi_{1,4,i}$ (d), $i = 1, 2, 3$.

TABLE V
Percentage of Range Bins for Dataset 1 Where Using Higher Order Statistics the SIRP Assumption Cannot Be Rejected for a 0.01 Significance Level

Test	N1	N2	N3
φ_1	99	98	99
φ_2	99	98	99
φ_3	99	99	99
φ_4	100	99	99
$\varphi_1 \wedge \varphi_2 \wedge \varphi_3 \wedge \varphi_4$	98	95	96

where $\varphi_{d,k,i}$ is the kth, $k = 1, \ldots, 4$, angular coordinate associated with the dataset d and the sensor node i, $d \in D$ and $i = 1, 2, 3$. In a nutshell, if the ECDFs of the angular coordinates adhere with the theoretical models in (8), then the SIRV assumption for $\boldsymbol{x}$ cannot be rejected. Before proceeding further, let us observe that the hypothesis test in (9) is not sensitive to possible covariance matrix changes since after the decimation process the underlying data spectrum is white (namely the covariance matrix is proportional to the identity matrix).

Using dataset 1, Fig. 5 displays the KS statistics obtained testing the generalized spherical coordinates $\varphi_{1,k,i}$, $k = 1, \ldots, 4$, $i = 1, 2, 3$, for each range bin belonging to the clutter patch along with the thresholds corresponding to 0.01 and 0.005 significance levels (dashed and solid line, respectively). The results show that most of the KS statistics are below the thresholds for both the bistatic and the monostatic measurements thus suggesting an overall compliance of the sea-clutter returns with the SIRV model. Each of the hypotheses in (9) represents a necessary condition for the data vector to be modeled as an SIRV. In this respect, Table V reports the percentage of range bins for which the SIRV hypothesis cannot be rejected, assuming a significance level of 0.01 for each angular coordinate test. Specifically, the first four rows refer to the results obtained testing each of the hypotheses $H_{0,k}$, $k = 1, \ldots, 4$, whereas the last refers to the percentage of range bins where all the four hypotheses cannot be rejected. Table VI, instead, for each angle coordinate gives the range bins for the different nodes where the corresponding KS statistic exceeds the decision threshold.

TABLE VI
Range Bins for Dataset 1 Where the Higher Order KS Statistics Exceed the Threshold for a 0.01 Significance Level

Statistic	N1	N2	N3
φ_1	130	72, 86, 142	99, 124
φ_2	59	100, 156, 157	96, 153
φ_3	3, 141	46	43
φ_4	-	153	100, 163

Interestingly, for each node, comparing the results of Tables III and VI, the range bins exceeding the threshold appear different. Hence, since both first- and higher order statistics represent necessary requirements for the compliance of the sea-clutter returns with the SIRP model, using both first- and higher order statistics the overall percentage of range bins agreeing with the SIRP model (evaluated considering $R \wedge \bar{R} \wedge \phi \wedge \varphi_1 \wedge \varphi_2 \wedge \varphi_3 \wedge \varphi_4$) is 97% for N1, 93% for N2, and 93% for N3.

2) *Coherence Time:* As already highlighted, the SIRP model represents a valuable description of the CG process within the coherence time T_c, i.e., the temporal interval where the texture component can be modeled as a random variable. Over such temporal scale, the clutter exhibits a local Gaussian behavior, namely the received data (under the SIRP assumption) can be deemed as a zero-mean complex circular Gaussian process with unknown variance. This observation paves the way to the design of an effective strategy to estimate T_c [44]. Specifically, T_c can be inferred from the available measurements by considering data sequences of increasing length (from both the quadrature components) and establishing whether the following hypothesis cannot be rejected:

$$H_{0,n} : \mathcal{P}\{z_{d,i}(t)\} \sim \mathcal{N}(0, \sigma_g^2), \quad t \in [0, T_n], \ n = 1, \ldots, N \tag{10}$$

$d \in D$, $i = 1, 2, 3$, where T_n is the temporal-duration of the nth sequence under test, σ_g^2 is the unknown variance parameter, and N is the total number of considered data sequences. In particular, T_n is progressively increased by 1.25 s, i.e., $T_n = n1.25$ s, $n = 1, \ldots, N$. Since the available data have been collected over a time span of 130 s, the total number of analyzed sequences is equal to 104. Besides, considering the decimation factor of 50 samples which, as discussed in Section III-A, ensures almost uncorrelated and hopefully almost independent speckle components, and the value of PRI, the shortest analyzed sequence (i.e., T_1) corresponds to 25 samples.

For each range bin of a specific dataset, the hypotheses $H_{0,n}, n = 1, \ldots, N$, can be tested by applying progressively the CV test [37] to the data belonging to the temporal interval $[0, T_n]$, $n = 1, \ldots, N$. It is expected that when the observation period becomes greater than the coherence length of the sequence, $H_{0,n}$ should be rejected and the

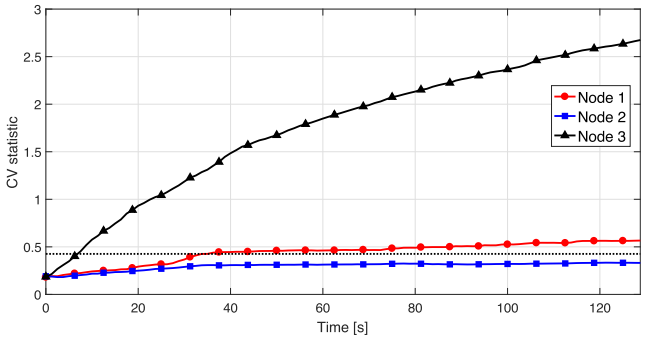

(a)

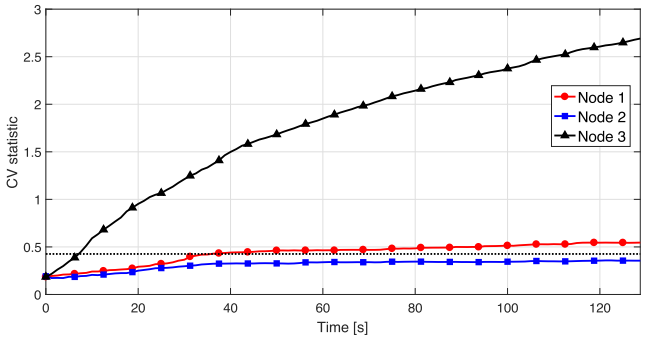

(b)

Fig. 6. Average coherence time evaluated over the (a) I and (b) Q components for dataset 1.

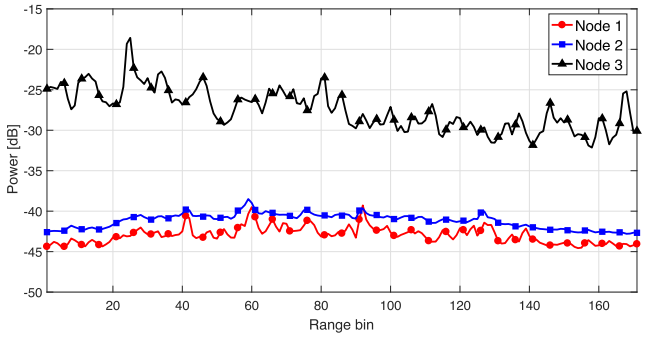

(a)

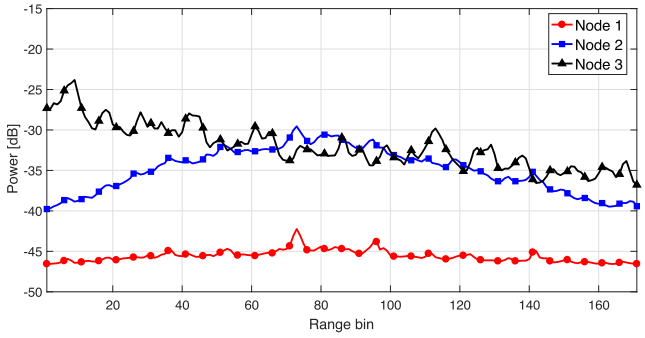

(b)

Fig. 7. Slow-time received power profile for dataset (a) 1 and (b) dataset 8.

texture component could be no longer modeled as a constant value.

Using the measurements from dataset 1, Fig. 6(a) and (b) shows the CV-distances versus the length of the analyzed temporal segments evaluated using the I and the Q components, respectively. Precisely, the reported CV distances have been averaged over the range bins belonging to the clutter patch for which both first- and higher order statistics comply with the SIRP model with a significance level of 0.01. Comparing the obtained results with the threshold at 0.01 significance level, it is possible to estimate the coherence time as the smallest T_n where the average CV distance exceeds the threshold, i.e., as the temporal-length after which the local Gaussian hypothesis has to be rejected. For the considered dataset, the plots point out that the estimated coherence time for the monostatic measurements is much smaller than the bistatic counterparts. Specifically, considering the measurements collected by N3 and N1, the estimated average coherence time (over the quadrature components) is about 6 s and 34 s, respectively. As to the cross-polarized signals, the □-marked blue curves of Fig. 6(a) and (b) reveal that the local Gaussian assumption cannot be rejected for the whole acquisition time. To the best of the authors' knowledge, this is a new and important achievement in the context of bistatic clutter characterization, which further sheds lights on the concept of clutter diversity [17], [18].

IV. RANGE AND POLARIMETRIC HETEROGENEITY

The goal of this section is twofold. First, the spatial heterogeneity characterizing both monostatic as well as bistatic radar echoes is investigated. Then, a cross-channel analysis is conducted to study the behavior of the textures and to assess the statistical independence of the speckle components (possibly related to different polarizations).

A. Spatial Heterogeneity

The spatial heterogeneity of the available measurements is analyzed using as performance metric the variance of the slow-time data, corresponding to the clutter power after compensating for a possible dc offset. Precisely, this analysis is conducted before data standardization evaluating the slow-time power profile over the range bins belonging to the clutter patch. To provide an illustrative example, Fig. 7 shows the results obtained assuming $\beta = 60^\circ$ and considering both horizontal and vertical polarizations at the transmit side (i.e., datasets 1 and 8, respectively). From the obtained behaviors, the following considerations can be drawn.

1) The measurements collected via N3 exhibit power range profiles with faster fluctuations (i.e., spatial variation of the clutter power) than those gathered using N1 and N2. This indicates a reduced degree of heterogeneity for the bistatic sensing mode.
2) At the passive nodes, the vertical co-polarized scenario [□-marked curve in Fig. 7(b)] shows a higher spatial variability, i.e., heterogeneity, than the horizontal co-polarized counterpart [o-marked curve in Fig. 7(a)]. Moreover, the vertical co-polarized bistatic returns exhibit higher power levels than the horizontal co-polarized counterparts agreeing with

the theory and the experimental evidence observed in the open literature for the monostatic configuration [34], [45], [46].

3) Regardless of the transmit polarization, the bistatic returns collected using the vertical polarized antenna (N2) are stronger than those acquired via the horizontal polarized counterpart (N1) [34].
4) The bistatic data achieve the highest power levels in correspondence of the range bins close to the center of the clutter patch (range bin 73).
5) As expected, the co-polarized measurements collected by N3 exhibit higher power levels than the cross-polarized counterparts [34].

B. Texture Analysis

The aim of the cross-channel analysis is to assess whether the bistatic sea-clutter returns from the same range cell acquired via N1 and N2 exhibit the same standardized texture component as well as to investigate the statistical independence of the corresponding speckles. To this end, let us observe that if the cross-polarized signals $z_{d,1}(n)$ and $z_{d,2}(n)$, $d \in D$, $n = 1, \ldots, N_s$, exhibit the same texture, then the ratio between arbitrary selected quadrature components on the two channels has to follow a standard Cauchy distribution. As a consequence, to assess whether the data collected by N1 and N2 possess the same texture and independent speckle components, the following simple hypothesis can be tested:

$$H_0 : \; R^{A,B}_{d,i,j}(n) = \frac{z^A_{d,i}(n)}{z^B_{d,j}(n)} \sim \mathcal{C}(0,1) \tag{11}$$

where $d \in D$, and the pairs $(i, j) \in \{(1,2),(2,1)\}$ and $(A, B) \in \{(I, I), (I, Q), (Q, I), (Q, Q)\}$, indicate the possible nodes and quadrature components combinations, respectively.

To support further the statistical independence of the speckle components observed at the passive sensors, a necessary requirement is the independence of the observations after a given transformation, which implies, in general, uncorrelation of the transformed data. This can be tested using the available measurements (which comprise both texture and speckle component), observing that under the SIRP assumption and independent speckles, the ratios

$$\frac{z^I_{d,1}(n)}{z^Q_{d,1}(n)}, \quad \frac{z^I_{d,2}(n)}{z^Q_{d,2}(n)}, \quad d \in D \tag{12}$$

have to be uncorrelated random variables. As a consequence cross-polarized speckle uncorrelation can be assessed considering the correlation index of the data warped according to the standard Cauchy distribution.

To provide an illustrative example, Fig. 8 shows the KS statistics obtained by testing the null hypothesis (11) along with the decision threshold at a 0.01 significance level for dataset 1. Inspection of the subplots highlights that the range bins corresponding to threshold crossing for $R^{AB}_{1,i,j}$ and $R^{AB}_{1,j,i}$, $(A, B) \in \{(I, I), (I, Q), (Q, I), (Q, Q)\}$, $i, j = 1, 2$ $(i \neq j)$, are substantially the same. Moreover,

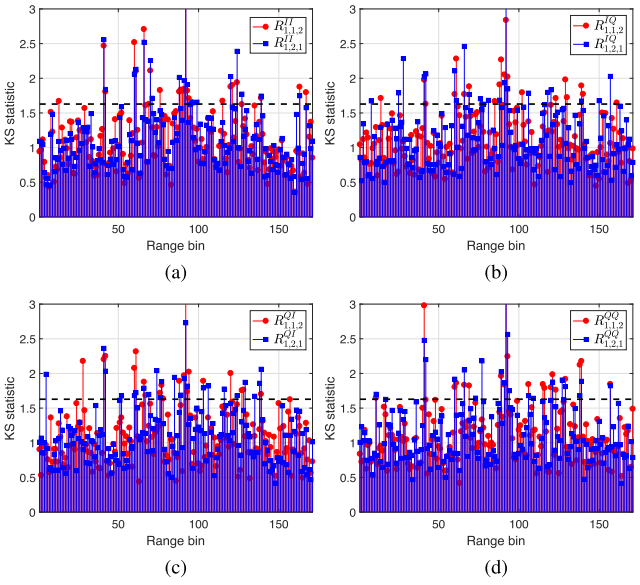

Fig. 8. KS statistics associated with $R^{II}_{1,i,j}$ (a), $R^{IQ}_{1,i,j}$ (b), $R^{QI}_{1,i,j}$ (c), $R^{QQ}_{1,i,j}$ (d), $(i, j) \in \{(1,2),(2,1)\}$.

67% KS statistics associated with the measurements from the range bins belonging to the clutter patch are below the decision threshold. This behavior agrees with the results of Fig. 6(a) and (b). In particular, while for N2 the CV statistics suggest that the quadrature components comply with a Gaussian distribution (□-marked red curves), for N1 the CV statistics are very close to the threshold (o-marked red curves), and hence, the quadrature components very slightly deviate from a Gaussian distribution. As a consequence, it is expected that the standardized texture component for N2 can be retained as a constant but unknown value over the whole acquisition time, whereas for N1 it just slightly changes over temporal intervals in the order of 34 s. Thus, the ratio between the textures over the cross-polarized channels is almost one, agreeing with the results reported in Fig. 8.

As to the speckle components, for all the sea-clutter returns associated with the range bins of the clutter patch, the evaluation of the correlation index of the warped ratios in (12) provide values lower than 0.06 ensuring uncorrelated and hopefully independent cross-polarized speckle components.

V. AGGREGATE RESULTS

In this section, the statistical tools presented in Section III to establish the adherence of the sea-clutter radar returns with the SIRP model are applied to all the available datasets in order to provide aggregate results.

As a first analysis, Table VII reports for each dataset the percentage of range bins where both first- and higher order statistics suggest the compatibility of the observed clutter returns with the SIRP model. The percentages are computed evaluating the number of range cells where the null hypotheses in (5), (6), and (9), cannot be rejected with a 0.01 significance level. Note that measurements from dataset 2 are not considered because the data acquired by

TABLE VII
Percentage of Range Bins Where, Using Both First- and Higher Order Statistics, the Compliance With the SIRP Model Cannot Be Rejected With a Significance Level of 0.01

Dataset	β	N1	N2	N3
1	60°	97	93	93
2	75°	N/A	N/A	N/A
4	90°	97	93	88
5	95°	98	90	93
6	105°	79	94	98
7	120°	91	97	94
8	60°	92	96	95
9	75°	94	97	92
11	90°	94	99	94
12	95°	95	98	89
13	105°	100	98	96
14	120°	100	36	91

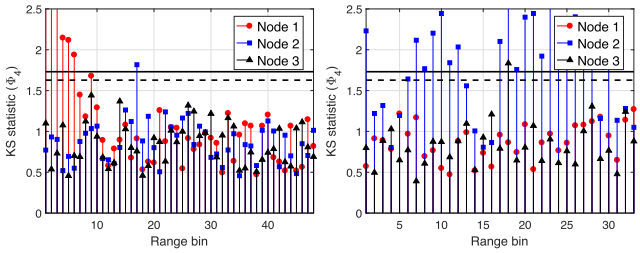

Fig. 9. KS statistics corresponding to $\varphi_{6,4,i}$ (a), $\varphi_{14,4,i}$, $i = 1, 2, 3$.

at least one of the three nodes was collected over a time window shorter than 130 s. This is the reason why the mentioned dataset is marked as not/analyzed (N/A).

With reference to the considered data, regardless the acquisition setup, the results highlight a good agreement between the monostatic sea-clutter returns and the SIRP model. As to the bistatic returns, the percentage of range bins where the compliance with the SIRP model cannot be rejected depends on both the polarization configuration and the bistatic angle. Table VII shows that, except for the co-polarized bistatic measurements of datasets 6 and 14, the data adhere well with a SIRP representation. To further shed light on the two situations where a significant number of deviations from the SIRP model occur, Fig. 9 shows the KS statistics corresponding to $\varphi_{d,4,i}$, $d = 6, 14$, $i = 1, 2, 3$. Inspection of Fig. 9(a) pinpoints that for dataset 6 most of the range bins exceeding the decision threshold are located at the beginning of the clutter patch. These range positions correspond also to the regions of the power range profile where high-power values are present [see Fig. 13(g)]. This is quite surprising being expected and reasonable that the power of the bistatic returns achieve small values at the edges of the clutter patch, due to antenna patterns, as it holds true in all the other situations (see the remaining plots of Figs. 13 and 14).

The next analysis is focused on the estimation of the coherence time resorting to the procedure illustrated in Section III-B2 for the dataset 1. Table VIII summarizes the results for all the considered datasets where c_I and c_Q indicate the coherence time estimated using the I and Q

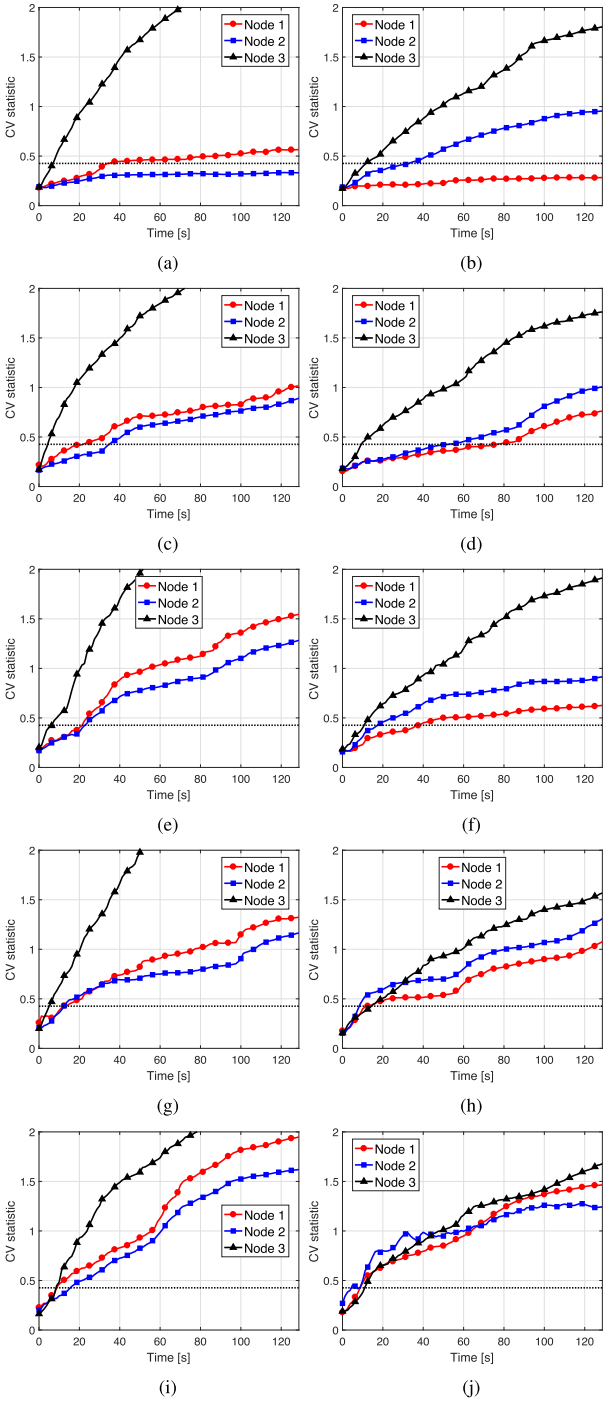

Fig. 10. CV statistics evaluated using the I component for (a) dataset 1, (b) dataset 8, (c) dataset 4, (d) dataset 11, (e) dataset 5, (f) dataset 12, (g) dataset 6, (h) dataset 13, (i) dataset 7, (j) dataset 14.

component, respectively, whereas c_{IQ} is the corresponding average. By analyzing the reported values, the following consideration can be drawn:

1) for each dataset and acquisition node c_I and c_Q almost coincide;
2) for both the horizontal and vertical co-polarized scenarios, at the passive side the estimated coherence time is smaller than the cross-polarized counterparts;

TABLE VIII
Average Coherence Time Evaluated Using Both the Quadrature Components

		N1			N2			N3		
Dataset	β [deg]	c_I [s]	c_Q [s]	c_{IQ} [s]	c_I [s]	c_Q [s]	c_{IQ} [s]	c_I [s]	c_Q [s]	c_{IQ} [s]
1	60°	35.0	36.3	35.6	-	-	-	7.5	7.5	7.5
2	75°	N/A	N/A	N/A	N/A	N/A	N/A	N/A	N/A	N/A
4	90°	22.5	27.5	25.0	35.0	35.0	35.0	5.0	3.8	4.4
5	95°	22.5	21.3	21.9	23.8	25.0	24.4	7.5	6.3	6.9
6	105°	12.5	11.3	11.9	12.5	13.8	13.1	6.3	6.3	6.3
7	120°	8.8	12.5	10.6	16.3	17.5	16.9	8.8	8.8	8.8
8	60°	-	-	-	33.8	31.3	32.5	12.5	12.5	12.5
9	75°	68.8	71.3	70.0	15.0	15.0	15.0	8.8	8.8	8.8
11	90°	77.5	76.3	76.9	52.5	50.0	51.3	10.0	10.0	10.0
12	95°	38.8	36.3	37.5	17.5	18.8	18.1	11.3	11.3	11.3
13	105°	12.5	12.5	12.5	8.8	8.8	8.8	15.0	12.5	13.8
14	120°	8.8	8.8	8.8	5.0	1.3	3.1	11.3	12.5	11.9

3) the measurements collected by N1 in co-polarized mode exhibit a coherence time that decreases as the bistatic angle increases;
4) for $\beta = 60°$ (the smallest considered bistatic angle) and cross-polarized bistatic sensing, the textures associated with the data acquired by N1 and N2 can be well approximated with a constant but unknown value over the whole acquisition interval;
5) using the vertical polarization at the active node, for $\beta = 105°$ and 120°, the bistatic cross-polarized sea-clutter returns at N1 exhibit a coherence time smaller than the monostatic one, see datasets 13 and 14.

A possible explanation about the general decreasing trend of the coherence time when β increases is connected with the different sizes of the clutter cells for the different bistatic angle configurations. Indeed, for the considered acquisition geometry, increasing β leads to a larger range cell, a higher grazing angle, and a lower bistatic range. Hence, the strength of the clutter return, with respect to the background noise, diminishes as β decreases. This implies that the measured data are represented better and better by a Gaussian model with a resulting larger and larger coherence time as β becomes smaller and smaller.

As a further evidence of the obtained results, Figs. 10–12, display the CV-distances defined in (10) versus the length of the analyzed temporal segments for N1, N2, and N3. Precisely, Figs. 10 and 11 refer to the I and Q components, respectively, for $\beta = 60°, 90°, 95°, 105°$, and 120°. Therein, for each bistatic angle, the plots on the left- and right-hand side consider the horizontal- and vertical-polarized transmit mode at N3, respectively. Fig. 12, instead, displays the CV-distances evaluated using the I and Q components of the measurements collected for $\beta = 75°$ and vertical-polarized transmit mode at N3 (the corresponding horizontal-polarized counterpart, i.e., dataset 2, is not analyzed).

Inspecting the aforementioned figures allows to quantify the actual deviation from the assumed local Gaussian behavior. This is a valuable information since, if the CV statistics are slightly above the decision threshold, it is possible to infer that the Gaussian model does well in the description of the clutter returns over the entire temporal window. Except for the case N2/dataset 14, the CV statistics associated with the co-polarized bistatic measurements (o-marked curves in the subplots (a), (c), (e), (g), and (i) of Figs. 10 and 11 for the horizontal polarization, □-marked curves in the subplots (b), (e), (h), and (j) of Figs. 10 and 11 and in Fig. 12 for the vertical one) are greater than those evaluated using the cross-polarized bistatic counterparts. Hence, for the co-polarized configuration, data present a local Gaussian behavior over a temporal period shorter than the cross-polarized observations. Moreover, the CV statistics for the bistatic data in the subplots (a) and (b) of Figs. 10 and 11 also suggest that, for $\beta = 60°$, data collected using cross-polarized channels agree with a Gaussian model with unknown variance over the whole observation interval.

To proceed with data assessment, Figs. 13 and 14 display the slow-time power profile (before standardization) over the range bins belonging to the clutter patch (for all the considered datasets). Inspection of the plots suggest that:

1) consistently with the results discussed for datasets 1 and 8 in Fig. 7, for all the considered sensing scenarios the bistatic sea-clutter returns on the horizontal polarization exhibit lower power levels than the vertical polarized counterparts;
2) while the power levels corresponding to the horizontal co-polarized acquisition on N3 are higher than the bistatic ones, the cross-polarized returns on N3 exhibit power levels comparable with those resulting from vertical co-polarized bistatic measurements (at least in a neighborhood of clutter patch center);
3) the power of the clutter echo increases as β increases.

The latter trend is due to the fact that, for the considered acquisition geometry, when the bistatic angle increases then the bistatic range decreases, the clutter cell area enlarges, and the reflectivity increases (as the grazing angle increases).

As to the texture analysis, for each dataset Table IX reports the percentages of range bins where the null hypothesis in (11) cannot be rejected with a significance level of 0.01. Specifically, for a given pair (i, j) of ordered bistatic nodes, the KS statistic in (11) is computed mixing all the quadrature components at the two nodes ($R^{II}_{d,i,j}, R^{IQ}_{d,i,j}, R^{QI}_{d,i,j}$,

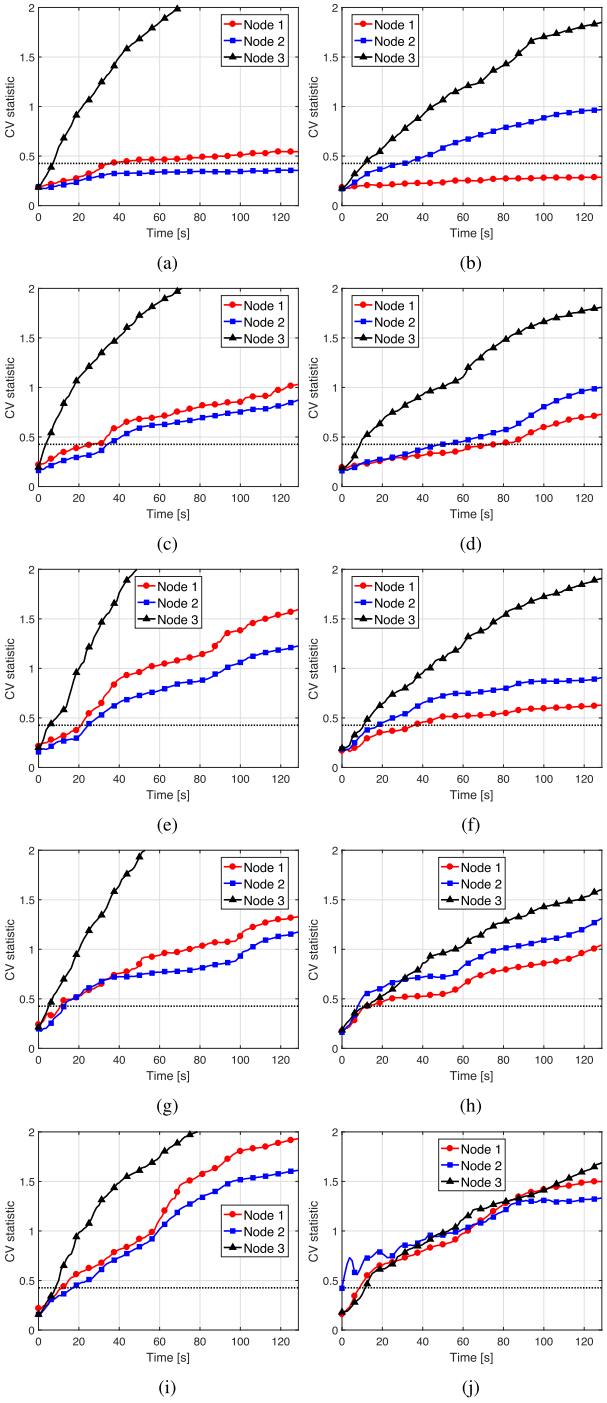

Fig. 11. CV statistics evaluated using the Q component for (a) dataset 1, (b) dataset 8, (c) dataset 4, (d) dataset 11, (e) dataset 5, (f) dataset 12, (g) dataset 6, (h) dataset 13, (i) dataset 7, (j) dataset 14.

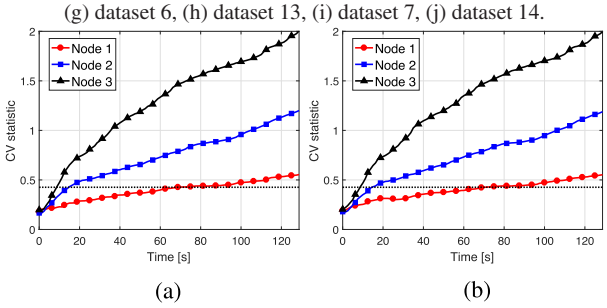

Fig. 12. CV statistics evaluated using the I (a) and the Q (b) component for dataset 9.

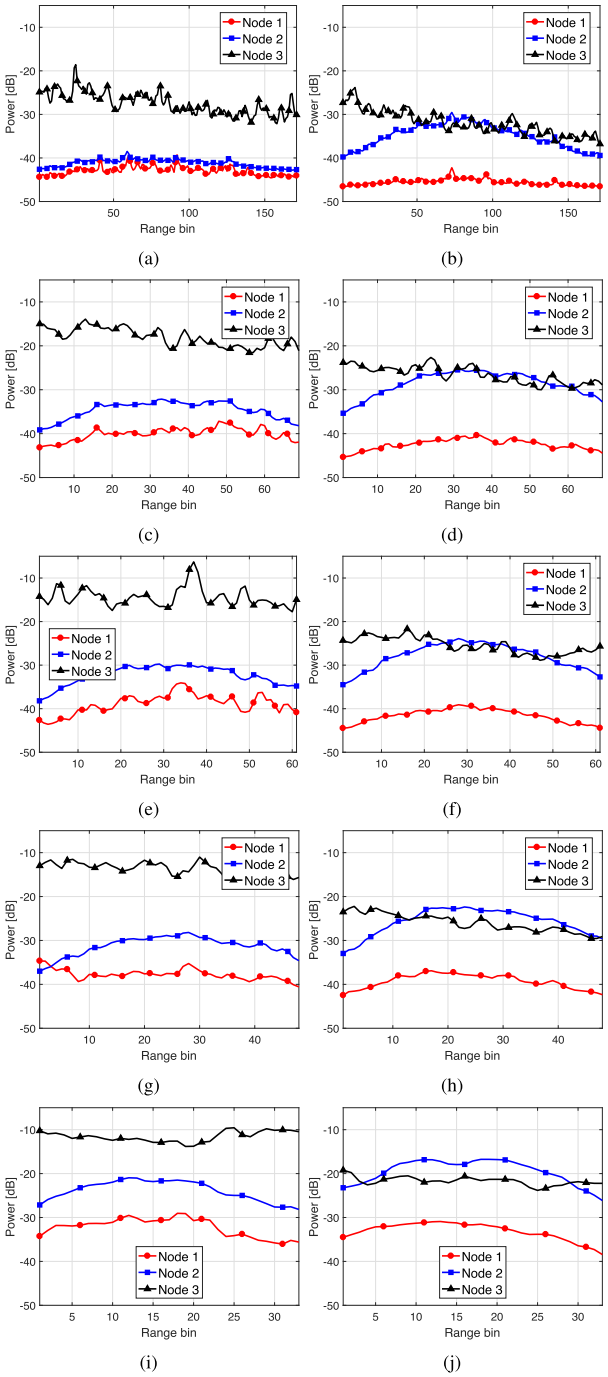

Fig. 13. Slow-time received power profile for (a) dataset 1, (b) dataset 8, (c) dataset 4, (d) dataset 11, (e) dataset 5, dataset 12, (g) dataset 6, (h) dataset 13, (i) dataset 7, (j) dataset 14.

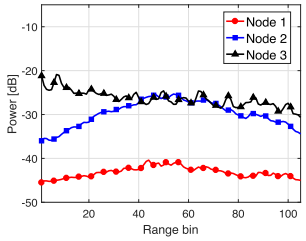

Fig. 14. Slow-time received power profile for dataset 9.

TABLE IX
Percentage of Range Bins Where, With a Significance Level of 0.01, the Standardized Data at N1 and N2 Share the Same Texture Components and Independent Speckles

Dataset	β	$\xi_{1,2}$	$\xi_{2,1}$	$\xi_{2,1} \wedge \xi_{2,1}$
1	60°	74	74	67
2	75°	N/A	N/A	N/A
4	90°	72	71	68
5	95°	49	49	41
6	105°	69	63	54
7	120°	64	73	64
8	60°	13	13	8
9	75°	8	9	5
11	90°	61	65	45
12	95°	75	62	56
13	105°	69	73	60
14	120°	30	21	18

and $R^{QQ}_{d,i,j}, d \in D$). Hence, for a given dataset, $\xi_{i,j}, i, j = 1, 2$ $(i \neq j)$ denotes the percentage of range bins where the four KS statistics do not exceed the decision threshold. The last column in Table IX, instead, refers to the overall percentage of range bins where the null hypothesis in (11) cannot be rejected according to all the necessary conditions tests, i.e., $\xi_{1,2} \wedge \xi_{2,1}$.

The obtained results clearly show that the behavior of the standardized textures at N1 and N2 depends on both the acquisition geometry and the transmit polarization. In particular, when N3 transmits horizontal-polarized signals, for values of β smaller than or equal to 90° the standardized textures over the cross-polarized bistatic channels can be retained almost the same, at least for the 67% of the range bins belonging to the clutter patch. Conversely, for the vertical-polarized transmit mode the opposite trend is observed, i.e., the standardized textures are substantially diverse.

Finally, to support the uncorrelation between the speckle components associated with the bistatic cross-polarized signals, the correlation index of the warped data provides values smaller than 0.08 for each of the considered experimental acquisitions, thus ensuring uncorrelated, and hopefully independent, speckles.

VI. CONCLUSION

This article has dealt with the statistical analysis of simultaneously recorded co- and cross-polarized bistatic coherent sea-clutter returns for different transmit polarizations and bistatic angles. This study has been first focused on establishing the agreement between the available measurements at each node and the SIRP model. To this end, both first- and higher order necessary conditions for the data to comply with the SIRP representation have been tested by the means of suitable statistical procedures leveraging on KS and CV tests. Besides, the spatial heterogeneity characterizing both monostatic and bistatic radar acquisitions has been analyzed in terms of power range profiles. Last but not least, a cross-channel analysis has been conducted to establish statistical dependency among the textures and the speckles observed at the different bistatic nodes.

With reference to the considered data, the analysis has highlighted a good level of SIRP compatibility with a coherence time at the bistatic nodes usually longer than the value measured by a simultaneously operating monostatic system. Moreover, while the coherence time at the monostatic node is only marginally affected by the acquisition configuration, that of the bistatic counterparts exhibit quite different values as a function of the bistatic angle and the transmit/receive polarization mode. As to the spatial heterogeneity, instead, regardless of the bistatic angle and the transmit polarization, the bistatic sea-clutter returns at the horizontal-polarized node show a lower power than the vertical polarized measurements. Finally, the cross-channel analyses reveal that for bistatic angles less than or equal to 90° the standardized textures over the cross-polarized bistatic channels can be deemed almost the same provided that horizontal-polarized pulses are transmitted. On the other hand, under vertical polarization on transmit the textures seem mostly uncorrelated. However, the conducted analysis has also highlighted that regardless of the transmit polarization, the similarity of the standardized textures over the bistatic channels increased as the bistatic angle increases from 95° to 105°.

Summarizing, the obtained results provide a novel experimental evidence on mutistatic/polarimetric clutter diversity as a function of both the acquisition geometry and the polarization, which can be exploited to boost radar target detection process. In particular, the gathered information about the statistical characteristics of the sea-clutter environment provides insights and guidelines toward the design of bespoke detection strategies capable of exploiting measurements collected simultaneously by monostatic and bistatic sensors and with polarimetric diversity. Moreover, the gathered knowledge on the texture coherence time paves the way for further clutter diversity assessments as, for instance, the investigation about the possible presence of relationships between the statistical parameters characterizing the returns on the different channels (such as the proportionality between the clutter covariance matrices on the two bistatic polarimetric channels). These studies are undoubtedly of interest and represent examples of possible future research directions.

ACKNOWLEDGMENT

The authors would like to thank the UCL and UCT team for collecting the data and making them available for this analysis. They would also like to thank the Associate Editor and the Referees for the interesting comments that have contributed to improve this article.

REFERENCES

[1] K. Ward, "Compound representation of high resolution sea clutter," *Electron. Lett.*, vol. 17, no. 2, pp. 561–563, Aug. 1981.
[2] S. Watts, "Radar detection prediction in k-distributed sea clutter and thermal noise," *IEEE Trans. Aerosp. Electron. Syst.*, vol. AES- 23, no. 1, pp. 40–45, Jan. 1987.
[3] E. Conte and M. Longo, "Characterisation of radar clutter as a spherically invariant random process," *IEE Proc. F. (Commun., Radar Signal Process.)*, vol. 134, pp. 191–197, Apr. 1987.

[4] K. Ward, C. Baker, and S. Watts, "Maritime surveillance radar. Part 1: Radar scattering from the ocean surface," *IEE Proc. F. (Radar Signal Process.)*, vol. 137, no. 11, pp. 51–62, Apr. 1990.
[5] H. Chan, "Radar sea-clutter at low grazing angles," *IEE Proc. F (Radar Signal Process.)*, vol. 137, no. 10, pp. 102–112, Apr. 1990.
[6] T. Nohara and S. Haykin, "Canadian east coast radar trials and the k-distribution," *IEE Proc. F. (Radar Signal Process.)*, vol. 138, no. 8, pp. 80–88, Apr. 1991.
[7] K. Sangston and K. Gerlach, "Coherent detection of radar targets in a non-Gaussian background," *IEEE Trans. Aerosp. Electron. Syst.*, vol. 30, no. 2, pp. 330–340, Apr. 1994.
[8] A. Farina, F. Gini, M. Greco, and L. Verrazzani, "High resolution sea clutter data: Statistical analysis of recorded live data," *IEE Proc.—Radar, Sonar Navigat.*, vol. 144, no. 9, pp. 121–130, Jun. 1997.
[9] P. Lombardo and D. Pastina, "Multiband coherent radar detection against compound-Gaussian clutter," *IEEE Trans. Aerosp. Electron. Syst.*, vol. 35, no. 4, pp. 1266–1282, Oct. 1999.
[10] I. Antipov, "Statistical analysis of northern australian coastline sea clutter data," Defence Science & Technology Organization, Edinburgh, SA, Australia, Tech. Rep. DSTO-TR-1236, 2001.
[11] F. Posner, "Spiky sea clutter at high range resolutions and very low grazing angles," *IEEE Trans. Aerosp. Electron. Syst.*, vol. 38, no. 1, pp. 58–73, Jan. 2002.
[12] E. Conte, A. De Maio, and C. Galdi, "Statistical analysis of real clutter at different range resolutions," *IEEE Trans. Aerosp. Electron. Syst.*, vol. 40, no. 3, pp. 903–918, Jul. 2004.
[13] M. Greco, F. Bordoni, and F. Gini, "X-band sea-clutter nonstationarity: Influence of long waves," *IEEE J. Ocean. Eng.*, vol. 29, no. 2, pp. 269–283, Apr. 2004.
[14] J. Carretero-Moya, J. Gismero-Menoyo, Blanco-del Campo, and A. Asensio-Lopez, "Statistical analysis of a high-resolution sea-clutter database," *IEEE Trans. Geosci. Remote Sens.*, vol. 48, no. 4, pp. 2024–2037, Apr. 2010.
[15] A. Mezache, F. Soltani, M. Sahed, and I. Chalabi, "Model for non-rayleigh clutter amplitudes using compound inverse Gaussian distribution: An experimental analysis," *IEEE Trans. Aerosp. Electron. Syst.*, vol. 51, no. 1, pp. 142–153, Jan. 2015.
[16] A. Fiche, S. Angelliaume, L. Rosenberg, and A. Khenchaf, "Analysis of x-band sar sea-clutter distributions at different grazing angles," *IEEE Trans. Geosci. Remote Sens.*, vol. 53, no. 8, pp. 4650–4660, Aug. 2015.
[17] H. D. Griffiths, "Keynote address: "clutter diversity: A new degree of freedom in multistatic radar," in *Proc. IEEE Radar Conf.*, 2014, pp. 11–11.
[18] R. Klemm, U. Nickel, C. Gierull, P. Lombardo, H. Griffiths, and W. Koch Eds., *Novel Radar Techniques and Applications: Waveform Diversity Cognitive Radar, Target Tracking Data Fusion (Radar, Sonar Navigation)*, vol. 2. London, U.K.: Inst. Eng. Technol., 2017.
[19] R. Klemm, U. Nickel, C. Gierull, P. Lombardo, H. Griffiths, and W. Koch Eds., *Novel Radar Techniques and Applications: Real Aperture Array Radar, Imaging Radar, and Passive and Multistatic Radar (Radar, Sonar and Navigation)*, vol. 1. London, U.K.: Inst. Eng. Technol., 2017.
[20] W. Al-Ashwal, "Measurement and modelling of bistatic sea clutter," Ph.D. dissertation, Dept. Electron. Elect. Eng., University College London, London, U.K., 2011.
[21] W. Al-Ashwal et al., "Statistical analysis of simultaneous monostatic and bistatic sea clutter at low grazing angles," *Electron. Lett.*, vol. 47, pp. 621–622, May 2011.
[22] W. A. Al-Ashwal et al., "Measurements of bistatic radar sea clutter," in *Proc. IEEE RadarConf.*, 2011, pp. 217–221.
[23] H. Griffiths, "Developments in bistatic and networked radar," in *Proc. IEEE CIE Int. Conf. Radar*, 2011, vol. 1, pp. 10–13.
[24] M. A. Ritchie, W. A. Al-Ashwal, A. G. Stove, K. Woodbridge, and H. D. Griffiths, "Statistical analysis of monostatic and bistatic sea clutter doppler spectrum," in *Proc. IEEE CIE Int. Conf. Radar*, 2011, vol. 1, pp. 816–820.
[25] M. A. Ritchie, W. A. Al-Ashwal, A. G. Stove, K. Woodbridge, and H. D. Griffiths Coherent analysis of horizontally-polarized monostatic and bistatic sea clutter," in *Proc. IET Int. Conf. Radar Syst.*, 2012, pp. 1–5.
[26] R. Palamà, M. Greco, P. Stinco, and F. Gini, "Statistical analysis of netrad high resolution sea clutter," in *Proc. 21st Eur. Signal Process. Conf.*, 2013, pp. 1–5.
[27] R. Palamà, M. Greco, P. Stinco, and F. Gini, "Analysis of sea spikes in netrad clutter," in *Proc. 11th Eur. Radar Conf.*, 2014, pp. 109–112.
[28] W. A. Al-Ashwal, K. Woodbridge, and H. D. Griffiths, "Analysis of bistatic sea clutter—Part I: Average reflectivity," *IEEE Trans. Aerosp. Electron. Syst.*, vol. 50, no. 2, pp. 1283–1292, Apr. 2014.
[29] W. A. Al-Ashwal, K. Woodbridge, and H. D. Griffiths, "Analysis of bistatic sea clutter—Part II: Amplitude statistics," *IEEE Trans. Aerosp. Electron. Syst.*, vol. 50, no. 2, pp. 1293–1303, Apr. 2014.
[30] R. Palamà, M. S. Greco, P. Stinco, and F. Gini, "Statistical analysis of bistatic and monostatic sea clutter," *IEEE Trans. Aerosp. Electron. Syst.*, vol. 51, no. 4, pp. 3036–3054, Oct. 2015.
[31] M. Ritchie, A. Stove, K. Woodbridge, and H. Griffiths, "Netrad: Monostatic and bistatic sea clutter texture and doppler spectra characterization at s-band," *IEEE Trans. Geosci. Remote Sens.*, vol. 54, no. 9, pp. 5533–5543, Sep. 2016.
[32] F. Fioranelli, M. Ritchie, H. Griffiths, S. Sandenbergh, and M. Inggs, "Analysis of polarimetric bistatic sea clutter using the netrad radar system," *IET Radar, Sonar Navigat.*, vol. 10, no. 8, pp. 1356–1366, 2016.
[33] R. Palamà et al., "Correlation analysis of simultaneously collected bistatic and monostatic sea clutter," in *Proc. IEEE Radar Conf.*, 2017, pp. 1466–1471.
[34] L. Rosenberg, S. Watts, and M. S. Greco, "Modeling the statistics of microwave radar sea clutter," *IEEE Aerosp. Electron. Syst. Mag.*, vol. 34, no. 10, pp. 44–75, Oct. 2019.
[35] S. Angelliaume, L. Rosenberg, and M. Ritchie, "Analysis of bistatic radar sea clutter amplitude distributions at low grazing angles," in *Proc. Int. Radar Conf.*, 2019, pp. 1–5.
[36] V. Carotenuto, A. Aubry, A. De Maio, and F. Fioranelli, "Multivariate polarimetric bistatic clutter statistical analysis," in *Proc. IEEE Radar Conf.*, 2022, pp. 1–6.
[37] R. D'Agostino and M. Stephens *Goodness-of-Fit Techniques*. New York, NY,USA: Marcel Dekker, 1986.
[38] N. Willis *Bistatic Radar (Radar, Sonar and Navigation)*. London, U.K.: Inst. Eng. Technol., 2004.
[39] M. Inggs et al., "Netrad multistatic sea clutter database," in *Proc. IEEE Int. Geosci. Remote Sens. Symp.*, 2012, pp. 2937–2940.
[40] M. R. Inggs, S. Lewis, R. Palamà, M. A. Ritchie, and H. Griffiths, "Report on the 2018 trials of the multistatic nextrad dual band polarimetric radar," in *Proc. IEEE Radar Conf.*, 2019, pp. 1–6.
[41] J. T. Nohara, "Detection of growlers in sea clutter using an x-band pulse-doppler radar," Ph.D. dissertation, McMaster University, Hamilton, ON, Canada 1991.
[42] K. Yao, "A representation theorem and its applications to spherically-invariant random processes," *IEEE Trans. Inf. Theory*, vol. IT-19, no. 5, pp. 600–608, Sep. 1973.
[43] E. Conte, M. Longo, and M. Lops, "Modelling and simulation of non-rayleigh radar clutter," *IEE Proc. F. (Radar Signal Process.)*, vol. 138, no. 9, pp. 121–130, Apr. 1991.
[44] E. Conte, M. Di Bisceglie, C. Galdi, and G. Ricci, "A procedure for measuring the coherence length of the sea texture," *IEEE Trans. Instrum. Meas.*, vol. 46, no. 4, pp. 836–841, Aug. 1997.
[45] K. Ward, R. Tough, and S. Watts *Sea Clutter: Scattering, the k Distribution and Radar Performance (Radar, Sonar and Navigation)*. London, U.K.: Inst. Eng. Technol., 2013.
[46] M. A. Richards, J. A. Scheer, and W. A. Holm Eds., *Principles of Modern Radar: Basic Principles (Radar, Sonar and Navigation)*. London, U.K.: Inst. Eng. Technol., 2010.

Augusto Aubry (Senior Member, IEEE) received the Dr. Eng. degree (Hons.) in telecommunication engineering and the Ph.D. degree in electronic and telecommunication engineering from the University of Naples Federico II, Naples, Italy, in 2007 and 2011, respectively.

From February to April 2012, he was a Visiting Researcher with the Hong Kong Baptist University, Hong Kong. He is currently an Associate Professor with the University of Naples Federico II. His research interests include statistical signal processing and optimization theory, with emphasis on topics related to MIMO communications and radar signal processing.

Dr. Aubry was the corecipient of the 2013 Best Paper Award (entitled to B. Carlton) of the IEEE Transactions on Aerospace and Electronic Systems with the contribution "Knowledge- Aided (Potentially Cognitive) Transmit Signal and Receive Filter Design in Signal-Dependent Clutter." He was the Recipient of the 2022 IEEE Fred Nathanson Memorial Award as the young (less than 40 years of age) AESS Radar Engineer 2022, with the following citation "For outstanding contributions to the application of modern optimization theory to radar waveform design and adaptive signal processing."

Vincenzo Carotenuto (Senior Member, IEEE) received the Dr. Eng. degree in telecommunication engineering and the Ph.D. degree in electronic and telecommunication engineering from the University of Naples Federico II, Naples, Italy, in 2010 and 2015, respectively.

He is currently under research agreement with the Department of Electrical and Information Technology Engineering, University of Naples Federico II. His research interest lies in the field of statistical signal processing, with an emphasis on radar signal processing.

Dr. Carotenuto is also the corecipient of the 2018 IEEE International Workshop on Metrology for Aerospace Best Radar Paper Award with the contribution "Assessing Spectral Compatibility Between Radar and Communication Systems on Measured Data."

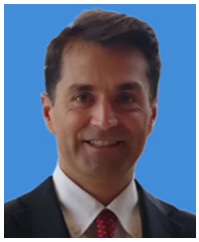

Antonio De Maio (Fellow, IEEE) received the Dr. Eng. (Hons.) and Ph.D. degrees in information engineering from the University of Naples Federico II, Naples, Italy, in 1998 and 2002, respectively.

From October to December 2004, he was a Visiting Researcher with the U.S. Air Force Research Laboratory, Rome, NY, USA. From November to December 2007, he was a Visiting Researcher with the Chinese University of Hong Kong, Hong Kong. He is currently a Professor with the University of Naples Federico II. His research interest lies in the field of statistical signal processing, with emphasis on radar detection, optimization theory applied to radar signal processing, and multiple-access communications.

Dr. Maio is the recipient of the 2010 IEEE Fred Nathanson Memorial Award as the young (less than 40 years of age) AESS Radar Engineer 2010 whose performance is particularly noteworthy as evidenced by contributions to the radar art over a period of several years, with the following citation for "robust CFAR detection, knowledge-based radar signal processing, and waveform design and diversity." He is the corecipient of the 2013 Best Paper Award (entitled to B. Carlton) of the IEEE TRANSACTIONS ON AEROSPACE AND ELECTRONIC SYSTEMS with the contribution "Knowledge-Aided (Potentially Cognitive) Transmit Signal and Receive Filter Design in Signal-Dependent Clutter."

Francesco Fioranelli (Senior Member, IEEE) received the Ph.D. degree from Durham University, Durham, U.K., in 2014.

He was an Assistant Professor with the University of Glasgow (2016–2019) and a Research Associate with the University College London, London, U.K., (2014–2016). He is currently a Tenured Assistant Professor with the TU Delft, Delft, The Netherlands. His research interests include the development of radar systems and automatic classification for human signatures analysis in healthcare and security, drones and UAVs detection and classification, automotive radar, wind farm, and sea clutter.